Electronic version of an article published as
International Journal of Computational Methods
Vol. 15, No. 5 (2018) 1850036 (35 pages)

DOI:10.1142/S0219876218500366
https://www.worldscientific.com/worldscinet/ijcm

THREE-DIMENSIONAL ELASTIC ANALYSIS OF A STRUCTURE WITH HOLES USING ACCELERATED COUPLING-MATRIX-FREE ITERATIVE S-VERSION FEM

YASUNORI YUSA

Department of Mechanical Engineering, Faculty of Science and Technology, Tokyo University of Science, 2641 Yamazaki, Noda, Chiba 278-8510, Japan
yyusa@rs.tus.ac.jp

HIROSHI OKADA

Department of Mechanical Engineering, Faculty of Science and Technology, Tokyo University of Science, 2641 Yamazaki, Noda, Chiba 278-8510, Japan

YOSUKE YUMOTO

Department of Mechanical Engineering, Graduate School of Science and Technology, Tokyo University of Science, 2641 Yamazaki, Noda, Chiba 278-8510, Japan

Received (11 April 2017)
Accepted (25 August 2017)

Some improvements of the coupling-matrix-free iterative s-version FEM to shorten its computational time are proposed. Then, the proposed method is applied to three-dimensional stress concentration problems. For sufficiently small computational time for practical use, two key techniques are introduced. First, the iteration is accelerated drastically by using the proposed convergence acceleration techniques. Secondly, stress transfers between global and local meshes is accelerated considerably by a bucket search algorithm. The proposed method was more than one hundred times faster than the straightforward algorithm of the coupling-matrix-free iterative s-version FEM.

Keywords: s-version finite element method; coupling stiffness matrix; three-dimensional solid finite element; fixed-point iteration method; quasi-Newton method; bucket search algorithm.

1. Introduction

Recently, three-dimensional finite element analysis of realistic structures has become very popular and common due to advances in computers. In such analysis, mesh generation of structures, especially structures with a local feature such as a hole or a crack, makes up the bulk of the analyst's efforts [Arai *et al.* (2015)]. The position

and the shape of a hole may change frequently in the design process. Moreover, the position and the shape of a crack are unknown until the crack is detected by non-destructive testing. The s-version finite element method (s-FEM) [Fish (1992); Fish and Markolefas (1993)] can reduce such efforts. In the s-FEM, a local mesh that represents a local feature such as a hole or a crack is superposed on a global mesh that represents the shape of a structure, as shown in Fig. 1. This local feature does not have to be modeled by the global mesh. Moreover, the position of the local mesh can easily be changed. The s-FEM has been applied to three-dimensional laminated composites [Fish and Guttal (1996)], three-dimensional particulate composites [Okada *et al.* (2004); Tanaka *et al.* (2006)], three-dimensional heterogeneous microstructures [Takano and Okuno (2004); Kawagai *et al.* (2006)] and three-dimensional crack propagation problems [Maitireyimu *et al.* (2009); Kamaya *et al.* (2010); Wada *et al.* (2014); Kikuchi *et al.* (2014)]. The crack propagation problems analyzed by Kikuchi *et al.* include mixed-mode cracks in specimens [Maitireyimu *et al.* (2009)], two interacting cracks [Kamaya *et al.* (2010)], complex-shape cracks [Wada *et al.* (2014)] and cracks in heterogeneous materials [Kikuchi *et al.* (2014)]. Nakasumi *et al.* [2003] demonstrated that a local mesh with solid finite elements can be superposed on a global mesh with shell finite elements. As mentioned above, the s-FEM can solve various three-dimensional elastic problems.

However, the s-FEM has a problem in that the generations of coupling stiffness matrices are troublesome. The coupling stiffness matrices, which represent the interactions between the global and local meshes, should be generated in the conventional s-FEM. In order to achieve a converged solution, accurate numerical integration for a partly overlapping region between a finite element of the global mesh and that of the local mesh, as shown in Fig. 2, needs to be carried out. Since the integrand has discontinuity on element faces, this numerical integration is very difficult to perform accurately, as long as Gaussian quadrature is used. Fish and Markolefas [1993] and Fish *et al.* [1994] divided a two-dimensional element into triangular and quadrangular elements. It would not be easy to apply this element subdivision technique to three-dimensional solid finite elements. Sando [2011a; 2011b] adopted the same strategy and performed this technique in a sophisticated manner using Delaunay triangulation. Lee *et al.* [2004] and Nakasumi *et al.* [2008] used high-order Gaussian quadratures with the assumption that the integrand outside the integration region is zero. Okada *et al.* [2005; 2007] and Kikuchi *et al.* [2008] divided an element uniformly. Okada *et al.* [2004] and Tanaka *et al.* [2006] proposed a sophisticated element subdivision technique by dividing an element recursively based on an octree. The high-order Gaussian quadrature and the uniform element subdivision have a high computational cost, especially in three-dimensional analysis.

In order to overcome this difficulty, the coupling-matrix-free iterative s-FEM was proposed by the present authors [Yumoto *et al.* (2016a; 2016b)] through fundamental studies based on two-dimensional problems. The coupling-matrix-free iterative

s-FEM uses stress transfers between global and local meshes rather than the generations of coupling stiffness matrices. A converged solution is achieved by iteration. Since the coupling-matrix-free iterative s-FEM consists only of conventional FEM analysis of each mesh and stress transfers, it would enable us to easily perform s-FEM analysis with general-purpose FEM software. The methodology is described in detail in the next section. Although an iterative s-FEM [Suzuki *et al.* (1999); Suzuki *et al.* (2002)] was proposed as a modification of the original s-FEM, it still requires the generations of coupling stiffness matrices. In this method, a 2×2 block linear system of equations of the original s-FEM is solved using an iterative method.

Here, several methods that use global and local models with iteration have been proposed for various purposes. Some methods use finite elements for both the global and local models, whereas other methods use an analytical solution, boundary elements, etc. The symmetric Galerkin boundary element method–finite element method (SGBEM–FEM) alternating method [Nikishkov *et al.* (2001); Han and Atluri (2002)] uses boundary elements to represent a crack and finite elements to represent the shape of a structure. The two analysis models are solved alternately, and a converged solution is obtained by iteration. Grm and Batista [2016] coupled an FEM solution and an analytical solution to analyze stress concentration problems very accurately. The iterative substructure method [Nishikawa *et al.* (2007)] was proposed for weld simulation. The local mesh is used to express strongly nonlinear mechanical phenomena near a heat source, whereas the global mesh is an elastic body. The two meshes are analyzed iteratively with assumed boundary conditions on the global–local interface in order to obtain a converged solution that satisfies both geometric continuity and force equilibrium. The partitioned coupling method [Yusa and Yoshimura (2013); Yusa and Yoshimura (2014)] uses non-overlapped global and local meshes and uses iterative nonlinear solvers, such as the fixed-point iteration method and the quasi-Newton method, to stabilize and accelerate convergence. Also, iterative methods have been used without global and local models. Zhang *et al.* [2016] used an iterative method to control the springback of sheet metal forming. In this method, the finite element analyses are performed many times. The domain decomposition method [Miyamura *et al.* (2002)] decomposes an FEM analysis model into multiple subdomains for parallel processing. Each subdomain is analyzed many times under the framework of the Newton–Raphson method with the preconditioned conjugate gradient method. Some of the above methods have been used to solve three-dimensional problems. Iterative methods are very effective especially in three-dimensional problems. This is why we also adopt an iterative method in the three-dimensional analysis of the present study.

In the present study, three-dimensional elastic problems with a single hole and with multiple holes are analyzed using the coupling-matrix-free iterative s-FEM, which was proposed by the authors through fundamental studies based on two-dimensional problems [Yumoto *et al.* (2016a; 2016b)]. This is the first study that three-dimensional problems have been analyzed by the coupling-matrix-free itera-

tive s-FEM. Although the original s-FEM can also analyze three-dimensional problems, the original s-FEM requires a very sophisticated numerical integration method that is particular to the s-FEM, especially in three dimensions. In contrast, the coupling-matrix-free iterative s-FEM does not require a hard task in programming, because the coupling stiffness matrices are no longer needed. The coupling-matrix-free iterative s-FEM consists only of conventional FEM analysis with initial stresses and stress transfers between the global and local meshes. This feature would enable us to perform s-FEM analysis by using commercial FEM software with its sophisticated features such as high-performance elements, multi-point constraints and contact. In the present paper, the capability of the coupling-matrix-free iterative s-FEM to analyze three-dimensional elastic problems with holes is demonstrated.

Although the formulation and the basic algorithm of the coupling-matrix-free iterative s-FEM was already proposed by the authors [Yumoto *et al.* (2016a; 2016b)], the effectiveness of the method should be enhanced in order to analyze three-dimensional problems in sufficiently small computational time for practical use. To accelerate the method, two key techniques are introduced. The two key techniques make the coupling-matrix-free iterative s-FEM comparable to the conventional FEM, in the sense of computational time. First, the iteration of the coupling-matrix-free iterative s-FEM is accelerated drastically by using convergence acceleration techniques. Although many of the methods reviewed in the present section use the straightforward global–local alternating algorithm, some of the methods [Suzuki *et al.* (1999; 2002); Yusa and Yoshimura (2013; 2014); Miyamura *et al.* (2002)] apply the algorithms of sophisticated linear and nonlinear solvers to their problems to stabilize and/or accelerate convergence. In the present study, in order to accelerate convergence, this technique is applied. Secondly, the search for neighboring integration points for the stress transfers between the global and local meshes is accelerated considerably by a bucket search algorithm [Ferrari *et al.* (2009); Murotani *et al.* (2014b)]. Although the two key techniques are based on conventional methods, they are highly tuned to fit the coupling-matrix-free iterative s-FEM. In this sense, the two key techniques are newly proposed in the present paper.

In the present paper, the methodology of the original s-FEM and the coupling-matrix-free iterative s-FEM are explained briefly, followed by the acceleration techniques. Then, using the present method, three-dimensional elastic problems are analyzed through numerical experiments. The accuracy and the convergence performance are investigated through simple stress concentration problems. Moreover, in order to demonstrate the capability of the coupling-matrix-free iterative s-FEM, three-dimensional structure models with a single hole and with multiple holes are analyzed. Also, the computational time is estimated and measured. It is shown that the coupling-matrix-free iterative s-FEM with holes is comparable in the sense of computational time to the conventional FEM without holes, even though the global and local meshes should be analyzed many times in the iteration. The total time for the analyst to perform manual operation from pre-processing to post-processing of

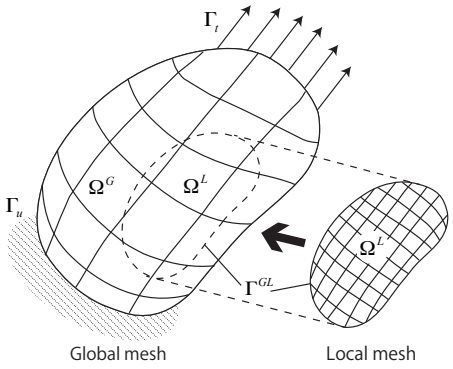

Fig. 1. Local mesh superposed on a global mesh.

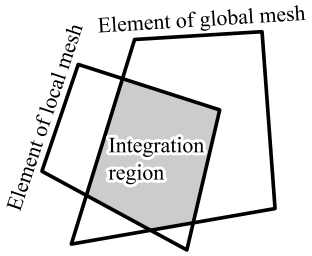

Fig. 2. Integration region to generate coupling stiffness matrices.

the coupling-matrix-free iterative s-FEM would be shorter than that of the conventional FEM when holes are added, because the effort involved in mesh generation is extremely small. According to Hughes *et al.* (2005), which is the proposal of isogeometric analysis, approximately 80% of analyst's time seems to be devoted to the mesh generation. Furthermore, it is demonstrated through numerical experiments that the shape, the position and the number of holes can be changed easily, whereas the global mesh remains unchanged.

2. Coupling-matrix-free iterative s-version FEM

In this section, the s-version finite element method (s-FEM) and the coupling-matrix-free iterative s-FEM are first outlined. Convergence acceleration techniques based on linear and nonlinear equation solution methods are then explained. Since three-dimensional finite element analysis tends to require a long computational time, the convergence acceleration techniques to reduce linear solver calls are needed in order to shorten the computational time. Moreover, effective use of linear solvers is indicated. Linear solvers are called at every iteration step of the coupling-matrix-free iterative s-FEM. The number of total iteration counts of iterative linear solvers strongly affects the computational time, which is reduced drastically by changing the procedures of the initial guess and the convergence criterion. Also, for the stress transfers in the coupling-matrix-free iterative s-FEM, a bucket search algorithm to collect neighboring integration points of the global and local meshes is introduced.

2.1. *S-version FEM*

In the s-version finite element method (s-FEM) [Fish (1992); Fish and Markolefas (1993)], a local mesh is superposed on a global mesh, as shown in Fig. 1. The local mesh represents a local feature such as a hole or a crack, whereas the global mesh represents the shape of the structure. A local domain, Ω^L, a global domain, Ω^G, and a global–local interface, Γ^{GL}, are defined. Γ_u and Γ_t designate the displacement-

and traction-prescribed boundaries. Here, continuous displacements, $\underset{\sim}{\boldsymbol{u}}$, are assumed to be

$$\underset{\sim}{\boldsymbol{u}} = \begin{cases} \underset{\sim}{\boldsymbol{u}}^G & \text{in } \Omega^G - \Omega^L, \\ \underset{\sim}{\boldsymbol{u}}^G + \underset{\sim}{\boldsymbol{u}}^L & \text{in } \Omega^L, \end{cases} \tag{1}$$

where $\underset{\sim}{\boldsymbol{u}}^G$ and $\underset{\sim}{\boldsymbol{u}}^L$ are continuous displacements on the global and local domains, respectively. In the present paper, we refer to these displacements as global and local continuous displacements, respectively. Other physical quantities such as global strains, $\boldsymbol{\varepsilon}^G$, local strains, $\boldsymbol{\varepsilon}^L$, global stresses, $\boldsymbol{\sigma}^G$, and local stresses, $\boldsymbol{\sigma}^L$, are referred to in a similar manner. In order to satisfy geometric continuity,

$$\underset{\sim}{\boldsymbol{u}}^L = 0 \text{ on } \Gamma^{GL}. \tag{2}$$

Strains, $\underset{\sim}{\boldsymbol{\varepsilon}}$, as well as the variations of displacements and strains, $\delta\underset{\sim}{\boldsymbol{u}}$ and $\delta\underset{\sim}{\boldsymbol{\varepsilon}}$, follow the superposition assumption of Eq. (1), because of the linear strain–displacement relation. Here, the principle of virtual work is introduced as

$$\int_{\Omega^G} \delta\underset{\sim}{\boldsymbol{\varepsilon}}^{\mathrm{T}} \boldsymbol{D} \underset{\sim}{\boldsymbol{\varepsilon}} \mathrm{d}\Omega = \int_{\Gamma_t} \delta\underset{\sim}{\boldsymbol{u}}^{\mathrm{T}} \boldsymbol{t} \mathrm{d}\Gamma + \int_{\Omega^G} \delta\underset{\sim}{\boldsymbol{u}}^{\mathrm{T}} \boldsymbol{b} \mathrm{d}\Omega, \tag{3}$$

where $\boldsymbol{D}$ is the elasticity matrix. Here, $\boldsymbol{t}$ and $\boldsymbol{b}$ are the prescribed traction and body forces, respectively. Inserting $\underset{\sim}{\boldsymbol{\varepsilon}} = \underset{\sim}{\boldsymbol{\varepsilon}}^G + \underset{\sim}{\boldsymbol{\varepsilon}}^L$, $\delta\underset{\sim}{\boldsymbol{u}} = \delta\underset{\sim}{\boldsymbol{u}}^G + \delta\underset{\sim}{\boldsymbol{u}}^L$, and $\delta\underset{\sim}{\boldsymbol{\varepsilon}} = \delta\underset{\sim}{\boldsymbol{\varepsilon}}^G + \delta\underset{\sim}{\boldsymbol{\varepsilon}}^L$ into Eq. (3), we derive

$$\int_{\Omega^G} \delta\underset{\sim}{\boldsymbol{\varepsilon}}^{G\mathrm{T}} \boldsymbol{D} \underset{\sim}{\boldsymbol{\varepsilon}}^G \mathrm{d}\Omega + \int_{\Omega^L} \delta\underset{\sim}{\boldsymbol{\varepsilon}}^{G\mathrm{T}} \boldsymbol{D} \underset{\sim}{\boldsymbol{\varepsilon}}^L \mathrm{d}\Omega = \int_{\Gamma_t} \delta\underset{\sim}{\boldsymbol{u}}^{G\mathrm{T}} \boldsymbol{t} \mathrm{d}\Gamma + \int_{\Omega^G} \delta\underset{\sim}{\boldsymbol{u}}^{G\mathrm{T}} \boldsymbol{b} \mathrm{d}\Omega \tag{4}$$

and

$$\int_{\Omega^L} \delta\underset{\sim}{\boldsymbol{\varepsilon}}^{L\mathrm{T}} \boldsymbol{D} \underset{\sim}{\boldsymbol{\varepsilon}}^G \mathrm{d}\Omega + \int_{\Omega^L} \delta\underset{\sim}{\boldsymbol{\varepsilon}}^{L\mathrm{T}} \boldsymbol{D} \underset{\sim}{\boldsymbol{\varepsilon}}^L \mathrm{d}\Omega = \int_{\Gamma_t} \delta\underset{\sim}{\boldsymbol{u}}^{L\mathrm{T}} \boldsymbol{t} \mathrm{d}\Gamma + \int_{\Omega^L} \delta\underset{\sim}{\boldsymbol{u}}^{L\mathrm{T}} \boldsymbol{b} \mathrm{d}\Omega. \tag{5}$$

Note that the surface of Ω^L can contain Γ_t as well as Γ_u, although it does not contain both Γ_t and Γ_u in Fig. 1. These equations are then discretized using $\delta\underset{\sim}{\boldsymbol{u}} = \boldsymbol{N}\delta\boldsymbol{u}$, $\underset{\sim}{\boldsymbol{\varepsilon}} = \boldsymbol{B}\boldsymbol{u}$, and $\delta\underset{\sim}{\boldsymbol{\varepsilon}} = \boldsymbol{B}\delta\boldsymbol{u}$. Here, $\boldsymbol{N}$ and $\boldsymbol{B}$ are the shape functions and the strain–displacement matrix, respectively. Moreover, $\boldsymbol{u}$ and $\delta\boldsymbol{u}$ are nodal discretized displacements and their variations, respectively. Hence, a linear system of equations,

$$\begin{bmatrix} \boldsymbol{K}^G & \boldsymbol{K}^{GL} \\ \boldsymbol{K}^{GL\mathrm{T}} & \boldsymbol{K}^L \end{bmatrix} \begin{Bmatrix} \boldsymbol{u}^G \\ \boldsymbol{u}^L \end{Bmatrix} = \begin{Bmatrix} \boldsymbol{f}^G \\ \boldsymbol{f}^L \end{Bmatrix}, \tag{6}$$

is obtained. Then, $\boldsymbol{K}^G = \int_{\Omega^G} \boldsymbol{B}^{G\mathrm{T}} \boldsymbol{D} \boldsymbol{B}^G \mathrm{d}\Omega$ is the stiffness matrix of the global mesh, and $\boldsymbol{K}^L = \int_{\Omega^L} \boldsymbol{B}^{L\mathrm{T}} \boldsymbol{D} \boldsymbol{B}^L \mathrm{d}\Omega$ is the stiffness matrix of the local mesh. Moreover, $\boldsymbol{K}^{GL} = \int_{\Omega^L} \boldsymbol{B}^{G\mathrm{T}} \boldsymbol{D} \boldsymbol{B}^L \mathrm{d}\Omega$ and $\boldsymbol{K}^{GL\mathrm{T}}$ are the coupling stiffness matrices. Also, $\boldsymbol{f}^G = \int_{\Gamma_t} \boldsymbol{N}^{G\mathrm{T}} \boldsymbol{t} \mathrm{d}\Gamma + \int_{\Omega^G} \boldsymbol{N}^{G\mathrm{T}} \boldsymbol{b} \mathrm{d}\Omega$ and $\boldsymbol{f}^L = \int_{\Gamma_t} \boldsymbol{N}^{L\mathrm{T}} \boldsymbol{t} \mathrm{d}\Gamma + \int_{\Omega^L} \boldsymbol{N}^{L\mathrm{T}} \boldsymbol{b} \mathrm{d}\Omega$

are the external force vectors of the global and local meshes, respectively. Finally, $\boldsymbol{u}^G$ and $\boldsymbol{u}^L$ are the global and local displacement vectors, respectively. The original s-FEM solves Eq. (6) monolithically. However, there is a difficulty in that the generations of the coupling stiffness matrices, $\boldsymbol{K}^{GL}$ and $\boldsymbol{K}^{GL^{\mathrm{T}}}$, require a lot of effort in program development. This is because the generations of $\boldsymbol{K}^{GL}$ and $\boldsymbol{K}^{GL^{\mathrm{T}}}$ require volume integration of two partly overlapping elements, as shown in Fig. 2. In order to obtain an accurate solution, a sophisticated numerical integration method that is particular to s-FEM is necessary [Fish and Markolefas (1993); Fish *et al.* (1994); Sando (2011a; 2011b); Lee *et al.* (2004); Nakasumi *et al.* (2008); Okada *et al.* (2004; 2005; 2007); Kikuchi *et al.* (2008); Tanaka *et al.* (2006)].

2.2. *Coupling-matrix-free iterative s-version FEM*

The coupling-matrix-free iterative s-version finite element method, which was proposed by the present authors [Yumoto *et al.* (2016a; 2016b)], does not require the generations of $\boldsymbol{K}^{GL}$ and $\boldsymbol{K}^{GL^{\mathrm{T}}}$. In this method, the multiplication of $\boldsymbol{K}^{GL}$ and $\boldsymbol{u}^L$ is evaluated implicitly as

$$\boldsymbol{\sigma}^L = \boldsymbol{D}\boldsymbol{B}^L\boldsymbol{u}^L \tag{7}$$

on the local mesh and then

$$\boldsymbol{K}^{GL}\boldsymbol{u}^L = \int_{\Omega^L} \boldsymbol{B}^G\boldsymbol{\sigma}^L \mathrm{d}\Omega \tag{8}$$

on the global mesh. Here, $\boldsymbol{\sigma}^L$ are local stresses, which are computed on the local mesh from the local displacements, $\boldsymbol{u}^L$, and are treated as initial stresses on the global mesh. Note that $\boldsymbol{\sigma}$ also follows the superposition assumption of Eq. (1). First, in the computational procedure, $\boldsymbol{\sigma}^L$ is computed by Eq. (7) at integration points of the local mesh. Then, $\boldsymbol{\sigma}^L$ is transferred from integration points of the local mesh to those of the global mesh using local least squares interpolation. In the local least squares interpolation, integration points of the local mesh inside a properly defined region are collected, and then $\boldsymbol{\sigma}^L$ at the integration points of the local mesh are interpolated to those of the global mesh. In the present study, the region is defined by the interior of an element of the global mesh, as shown in Fig. 3 (left). Element edges and integration points of the global mesh are shown in black, whereas those of the local mesh are shown in dark gray. The light gray element of the local mesh is the region in which interpolations are performed. Also, in the present study, a linear basis function,

$$f(\boldsymbol{x}) = \alpha_0 + \alpha_1 x + \alpha_2 y + \alpha_3 z, \tag{9}$$

is adopted. Here, $\boldsymbol{x} = [x\ y\ z]^{\mathrm{T}}$ are the relative coordinates from the destination integration point of the global mesh, and α_0, α_1, α_2 and α_3 are the coefficients. Using this function, the x-component of the local stresses at the destination integration point of the global mesh is calculated as $f(\boldsymbol{0})$ with minimal $\sum_i \left[\sigma_x^L(\boldsymbol{x}_i) - f(\boldsymbol{x}_i)\right]^2$,

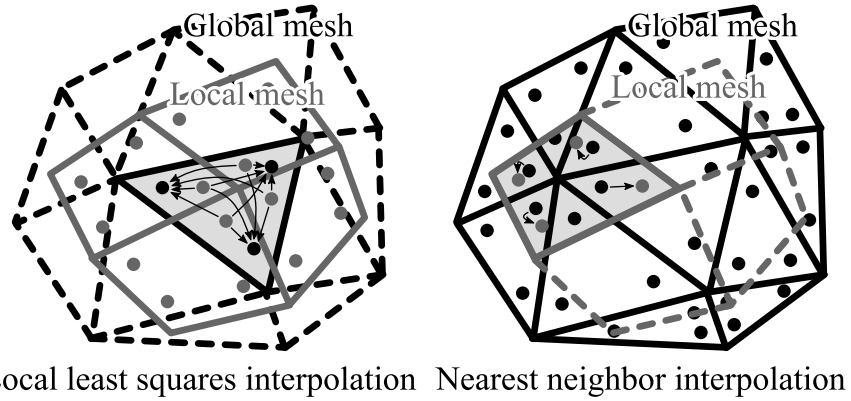

Fig. 3. Stress transfers between integration points of the global and local meshes.

where i is every integration point of the local mesh inside the defined region. The other components of the local stresses are calculated in a similar manner. Finally, $\boldsymbol{K}^{GL}\boldsymbol{u}^{L}$ is computed by Eq. (8) on the global mesh. Note that the coupling-matrix-free iterative s-FEM is equivalent to the conventional s-FEM if every integration point of the local mesh is at the same location as the corresponding integration point of the global mesh and copy-based stress transfers are used. In the present study, we select the independence of the global and local analyses rather than the equivalence to the conventional s-FEM.

The multiplication of $\boldsymbol{K}^{GL^{\mathrm{T}}}$ and $\boldsymbol{u}^{G}$ is computed in a similar fashion. To transfer $\boldsymbol{\sigma}^{G}$, nearest neighbor interpolation is used. $\boldsymbol{\sigma}^{G}$ are copied to the integration point of the local mesh from the nearest integration point of the global mesh, as shown in Fig. 3 (right).

In the previous study, the pair of these two interpolations showed good performance in terms of accuracy [Yumoto *et al.* (2016a)]. Any finite element type can be used without any additional techniques, because only the shapes of elements as polyhedrons are used in the stress transfers. In the present study, the hexahedral and tetrahedral finite elements are used simultaneously in the numerical experiments.

In the coupling-matrix-free iterative s-FEM, Eq. (6) is regarded as a 2×2 block linear system and is solved iteratively. Convergence at the kth iteration step is checked by

$$\frac{\left\| \begin{Bmatrix} \boldsymbol{f}^{G} \\ \boldsymbol{f}^{L} \end{Bmatrix} - \begin{bmatrix} \boldsymbol{K}^{G} & \boldsymbol{K}^{GL} \\ \boldsymbol{K}^{GL^{\mathrm{T}}} & \boldsymbol{K}^{L} \end{bmatrix} \begin{Bmatrix} \boldsymbol{u}^{G^{(k)}} \\ \boldsymbol{u}^{L^{(k)}} \end{Bmatrix} \right\|}{\left\| \begin{Bmatrix} \boldsymbol{f}^{G} \\ \boldsymbol{f}^{L} \end{Bmatrix} \right\|} = \frac{\left\| \begin{Bmatrix} \boldsymbol{f}^{G} - \boldsymbol{K}^{G}\boldsymbol{u}^{G^{(k)}} - \int_{\Omega^{L}} \boldsymbol{B}^{G}\boldsymbol{\sigma}^{L^{(k)}} \mathrm{d}\Omega \\ \boldsymbol{f}^{L} - \int_{\Omega^{L}} \boldsymbol{B}^{L}\boldsymbol{\sigma}^{G^{(k)}} \mathrm{d}\Omega - \boldsymbol{K}^{L}\boldsymbol{u}^{L^{(k)}} \end{Bmatrix} \right\|}{\left\| \begin{Bmatrix} \boldsymbol{f}^{G} \\ \boldsymbol{f}^{L} \end{Bmatrix} \right\|} \leq \tau, \tag{10}$$

where τ is a tolerance parameter.

2.3. *Convergence acceleration techniques*

In the present study, in order to shorten the computational time of three-dimensional finite element analysis, convergence acceleration techniques are applied to the coupling-matrix-free iterative s-FEM. These techniques are based on linear and nonlinear equation solution methods. In the present study, the following five linear and nonlinear solution methods are considered.

- Gauss–Seidel method
- Successive over-relaxation (SOR) method
- Gauss–Seidel method with the fixed-point iteration method and static relaxation
- Gauss–Seidel method with the fixed-point iteration method and Aitken relaxation
- Gauss–Seidel method with the limited-memory Broyden method

The Gauss–Seidel method is the straightforward method, which was also used in the previous study [Yumoto *et al.* (2016a; 2016b)]. In the Gauss–Seidel method, Eq. (6) is solved iteratively as

$$\begin{aligned} \boldsymbol{u}^{G(k+1)} &= \boldsymbol{K}^{G^{-1}} \left(\boldsymbol{f}^G - \boldsymbol{K}^{GL} \boldsymbol{u}^{L(k)} \right) \\ &= \boldsymbol{K}^{G^{-1}} \left(\boldsymbol{f}^G - \int_{\Omega^L} \boldsymbol{B}^G \boldsymbol{\sigma}^{L(k)} \mathrm{d}\Omega \right) \end{aligned} \tag{11}$$

and

$$\begin{aligned} \boldsymbol{u}^{L(k+1)} &= \boldsymbol{K}^{L^{-1}} \left(\boldsymbol{f}^L - \boldsymbol{K}^{GL^{\mathrm{T}}} \boldsymbol{u}^{G(k+1)} \right) \\ &= \boldsymbol{K}^{L^{-1}} \left(\boldsymbol{f}^L - \int_{\Omega^L} \boldsymbol{B}^L \boldsymbol{\sigma}^{G(k+1)} \mathrm{d}\Omega \right), \end{aligned} \tag{12}$$

where k is the iteration step. These two equations are solved alternately until the converged solution is achieved.

The successive over-relaxation (SOR) method uses a relaxation factor, ω, as

$$\begin{aligned} \boldsymbol{u}^{G(k+1)} &= (1-\omega)\, \boldsymbol{u}^{G(k)} + \omega \boldsymbol{K}^{G^{-1}} \left(\boldsymbol{f}^G - \boldsymbol{K}^{GL} \boldsymbol{u}^{L(k)} \right) \\ &= (1-\omega)\, \boldsymbol{u}^{G(k)} + \omega \boldsymbol{K}^{G^{-1}} \left(\boldsymbol{f}^G - \int_{\Omega^L} \boldsymbol{B}^G \boldsymbol{\sigma}^{L(k)} \mathrm{d}\Omega \right) \end{aligned} \tag{13}$$

and

$$\begin{aligned} \boldsymbol{u}^{L(k+1)} &= (1-\omega)\, \boldsymbol{u}^{L(k)} + \omega \boldsymbol{K}^{L^{-1}} \left(\boldsymbol{f}^L - \boldsymbol{K}^{GL^{\mathrm{T}}} \boldsymbol{u}^{G(k+1)} \right) \\ &= (1-\omega)\, \boldsymbol{u}^{L(k)} + \omega \boldsymbol{K}^{L^{-1}} \left(\boldsymbol{f}^L - \int_{\Omega^L} \boldsymbol{B}^L \boldsymbol{\sigma}^{G(k+1)} \mathrm{d}\Omega \right). \end{aligned} \tag{14}$$

The SOR method requires a parametric study on ω. It is known that $0 < \omega < 2$ is necessary to obtain a converged solution in the SOR method.

However, ω can be introduced in another way. From Eqs. (11) and (12), $\boldsymbol{u}^G$ can be eliminated, and a residual vector, $\boldsymbol{r}$, is defined in the present study as

$$\begin{aligned}\boldsymbol{r} &= \boldsymbol{u}^L - \boldsymbol{K}^{L^{-1}}\left(\boldsymbol{f}^L - \boldsymbol{K}^{GL^{\mathrm{T}}}\boldsymbol{u}^G\right)\\ &= \boldsymbol{u}^L - \boldsymbol{K}^{L^{-1}}\left(\boldsymbol{f}^L - \boldsymbol{K}^{GL^{\mathrm{T}}}\boldsymbol{K}^{G^{-1}}\left(\boldsymbol{f}^G - \boldsymbol{K}^{GL}\boldsymbol{u}^L\right)\right)\\ &= \boldsymbol{u}^L - \boldsymbol{K}^{L^{-1}}\left(\boldsymbol{f}^L - \int_{\Omega^L}\boldsymbol{B}^L\boldsymbol{D}\boldsymbol{B}^G\boldsymbol{K}^{G^{-1}}\left(\boldsymbol{f}^G - \int_{\Omega^L}\boldsymbol{B}^G\boldsymbol{D}\boldsymbol{B}^L\boldsymbol{u}^L\mathrm{d}\Omega\right)\mathrm{d}\Omega\right)\end{aligned} \tag{15}$$

Then, a system of equations to be solved about $\boldsymbol{u}^L$ is derived as

$$\boldsymbol{r} = \boldsymbol{0}. \tag{16}$$

This equation can be solved by nonlinear solution methods, such as the fixed-point iteration method and quasi-Newton methods. The fixed-point iteration method updates the unknown vector, $\boldsymbol{u}^L$, by

$$\boldsymbol{u}^{L^{(k+1)}} = \boldsymbol{u}^{L^{(k)}} - \boldsymbol{r}^{(k+1)}. \tag{17}$$

This update is equivalent to the Gauss–Seidel method given by Eqs. (11) and (12). The relaxation factor, ω, is introduced as

$$\boldsymbol{u}^{L^{(k+1)}} = \boldsymbol{u}^{L^{(k)}} - \omega\boldsymbol{r}^{(k+1)}. \tag{18}$$

This method also requires a parametric study on ω. $0 < \omega < 2$ would also be necessary to obtain a converged solution in the Gauss–Seidel method with relaxation.

Optimal ω can be estimated automatically at every iteration step by the Aitken method [Minami and Yoshimura (2009; 2010); Yusa and Yoshimura (2013)], which is based on the secant method. In the Aitken method, $\omega^{(k+1)}$ is estimated by

$$\omega^{(k+1)} = \underset{\omega^{(k+1)}}{\arg\min}\left\|\Delta\boldsymbol{u}^{L^{(k)}} - \omega^{(k+1)}\left(\boldsymbol{r}^{(k+1)} - \boldsymbol{r}^{(k)}\right)\right\|, \tag{19}$$

where

$$\Delta\boldsymbol{u}^{L^{(k)}} = \boldsymbol{u}^{L^{(k)}} - \boldsymbol{u}^{L^{(k-1)}}. \tag{20}$$

The term in $\arg\min\|\|$ of the right-hand side is reduced to a scalar by multiplying $\boldsymbol{r}^{(k+1)} - \boldsymbol{r}^{(k)}$. Then, $\arg\min\|\|$ is solved as

$$\omega^{(k+1)} = \frac{\Delta\boldsymbol{u}^{L^{(k)^{\mathrm{T}}}}\left(\boldsymbol{r}^{(k+1)} - \boldsymbol{r}^{(k)}\right)}{\left\|\boldsymbol{r}^{(k+1)} - \boldsymbol{r}^{(k)}\right\|^2}. \tag{21}$$

In the present study, the initial guess of the relaxation factor, $\omega^{(0)}$, is assumed to be unity.

Equation (16) can also be solved by quasi-Newton methods. Quasi-Newton methods update the unknown vector, $\boldsymbol{u}^L$, by

$$\boldsymbol{u}^{L^{(k+1)}} = \boldsymbol{u}^{L^{(k)}} - \boldsymbol{J}^{(k+1)^{-1}}\boldsymbol{r}^{(k+1)}. \tag{22}$$

$\boldsymbol{J}$ is the approximate Jacobian matrix, i.e.,

$$\boldsymbol{J} \approx \frac{\partial \boldsymbol{r}}{\partial \boldsymbol{u}^L}. \tag{23}$$

In the present study, the Broyden method [Kelley (2003); Minami and Yoshimura (2009; 2010); Yusa and Yoshimura (2014)], which is a quasi-Newton method, is tested. The Broyden method updates $\boldsymbol{J}$ by

$$\boldsymbol{J}^{(k+1)} = \boldsymbol{J}^{(k)} + \frac{\boldsymbol{r}^{(k+1)} \Delta \boldsymbol{u}^{L^{(k)\mathrm{T}}}}{\left\| \Delta \boldsymbol{u}^{L^{(k)}} \right\|^2}. \tag{24}$$

Although this equation can be used directly, the limited-memory method [Kelley (2003)] is used in order to reduce the memory usage and the computational cost of the large dense matrix, $\boldsymbol{J}$. The limited-memory method replaces the multiplications of $\boldsymbol{J}$ and vectors by vector operations. Here, the Sherman–Morrison formula, is introduced as

$$\left(\boldsymbol{M} + \boldsymbol{u}\boldsymbol{v}^{\mathrm{T}}\right)^{-1} = \left(\boldsymbol{I} - \frac{\boldsymbol{M}^{-1}\boldsymbol{u}}{1 + \boldsymbol{v}^{\mathrm{T}}\boldsymbol{M}^{-1}\boldsymbol{u}}\boldsymbol{v}^{\mathrm{T}}\right)\boldsymbol{M}^{-1}, \tag{25}$$

where $\boldsymbol{M}$ is an arbitrary matrix, $\boldsymbol{u}$ and $\boldsymbol{v}$ are arbitrary vectors, and $\boldsymbol{I}$ is the identity matrix. By carefully applying this formula to Eq. (24), we can derive

$$\Delta \boldsymbol{u}^{L^{(k+1)}} = -{\boldsymbol{J}^{(k+1)}}^{-1} \boldsymbol{r}^{(k+1)} = \frac{\boldsymbol{p}^{(k+1,k)}}{1 - \frac{\Delta \boldsymbol{u}^{L^{(k)\mathrm{T}}} \boldsymbol{p}^{(k+1,k)}}{\left\| \Delta \boldsymbol{u}^{L^{(k)}} \right\|^2}} \tag{26}$$

and

$$\boldsymbol{p}^{(k+1,i+1)} = -{\boldsymbol{J}^{(i+1)}}^{-1} \boldsymbol{r}^{(k+1)} = \boldsymbol{p}^{(k+1,i)} + \frac{\Delta \boldsymbol{u}^{L^{(i)\mathrm{T}}} \boldsymbol{p}^{(k+1,i)}}{\left\| \Delta \boldsymbol{u}^{L^{(i)}} \right\|^2} \Delta \boldsymbol{u}^{L^{(i+1)}}. \tag{27}$$

These equations are evaluated recursively in the computational procedure. In the present study, the initial guess of the approximate Jacobian matrix, $\boldsymbol{J}^{(0)}$, is assumed to be the identity matrix.

The algorithm of the five methods mentioned above is summarized as follows.

$\boldsymbol{u}^{L^{(0)}} \leftarrow \boldsymbol{0}$ (initial guess)
$k \leftarrow 0$
repeat
  Compute $\boldsymbol{u}^{G^{(k+1)}}$ by Eq. (11) or (13) (global analysis)
  Compute $\boldsymbol{u}^{L^{(k+1)}}$ by Eq. (12) or (14) (local analysis)
  Compute $\boldsymbol{r}^{(k+1)}$ by Eq. (15)
  Recompute $\boldsymbol{u}^{L^{(k+1)}}$ by Eq. (17), (18) or (22)
  $k \leftarrow k + 1$
until Eq. (10) is met

Note that this alternating procedure of global and local analyses is the same for the five methods.

2.4. *Effective use of linear solvers*

In the present study, an LDL factorization solver is used for local analysis and a preconditioned conjugate gradient (PCG) solver is used for global analysis. When the target problem is a real complex-shaped structure, the local mesh remains small scale, whereas the global mesh tends to become large scale. In the small-scale analysis, the use of direct linear solvers, as in the LDL factorization method, is preferable, whereas the use of iterative linear solvers, as in the PCG method, is preferable in the large-scale analysis. These linear solvers are called at every iteration step of the coupling-matrix-free iterative s-FEM. In this subsection, effective use of LDL factorization and PCG solvers to reduce computational time is indicated.

An LDL factorization solver with a skyline matrix is used for local analysis. The LDL factorization method consists of the phases of factorization and triangular solution (forward and backward substitutions). Note that this feature is general for factorization-based direct linear solvers, such as LU and LL factorization methods with skyline as well as sparse matrices. The factorization procedure can be performed only once at the first iteration step of the coupling-matrix-free iterative s-FEM, whereas the triangular solution procedure must be performed at every iteration step. This is because the stiffness matrix of the local mesh, $\boldsymbol{K}^L$, remains constant throughout the analysis. Only the right-hand-side vector changes.

A PCG solver with a symmetric compressed sparse row (CSR) matrix is used for global analysis. The matrix–vector multiplication and the vector operations are parallelized using OpenMP. The preconditioner of incomplete Cholesky factorization with zero fill-in (IC (0)) is adopted. Similarly to the LDL factorization solver, the phase of incomplete Cholesky factorization is performed only once at the first iteration step of the coupling-matrix-free iterative s-FEM. In addition, the procedures of the initial guess and the convergence criterion are changed in order to drastically reduce the total PCG iteration count. This technique is similar to Miyamura *et al.* [Miyamura *et al.* (2002)] in which the PCG solver is called at every Newton–Raphson iteration step. Let us assume a linear system to be solved as

$$\boldsymbol{K}\boldsymbol{u} = \boldsymbol{f} \tag{28}$$

and its residual vector as

$$\boldsymbol{r} = \boldsymbol{f} - \boldsymbol{K}\boldsymbol{u}. \tag{29}$$

In the straightforward use of a PCG solver, the relative residual norm, $\|\boldsymbol{r}\| / \|\boldsymbol{f}\|$, starts with 10^0, because of $\boldsymbol{u}^{(0)} = \boldsymbol{0}$, and ends with $\leq \varepsilon$. Here, ε is the tolerance parameter, which should probably be smaller than τ in Eq. (10). However, this use is somewhat wasteful. In the present study, the initial guess, $\boldsymbol{u}^{(0)}$, is set to be the converged solution at the previous iteration step of the coupling-matrix-free iterative s-FEM. This initial guess would be nearer to the converged solution than the zero vector. Moreover, we use

$$\frac{\left\|\boldsymbol{r}^{(k)}\right\|}{\left\|\boldsymbol{r}^{(0)}\right\|} \leq \varepsilon \tag{30}$$

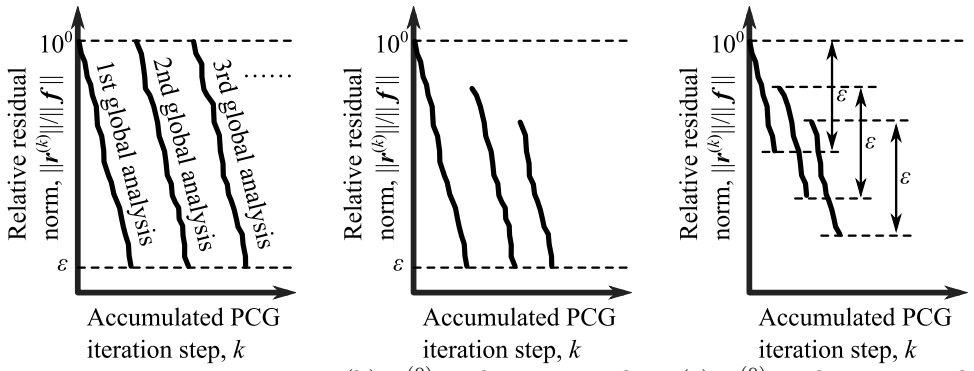

(a) $\boldsymbol{u}^{(0)} = \boldsymbol{0}$ and the convergence criterion is Eq. (31).

(b) $\boldsymbol{u}^{(0)}$ is the converged solution at the previous iteration step and the convergence criterion is Eq. (31).

(c) $\boldsymbol{u}^{(0)}$ is the converged solution at the previous iteration step and the convergence criterion is Eq. (30).

Fig. 4. Changes of the initial guess and the convergence criterion of a PCG solver for the global analysis.

as the convergence criterion at the kth PCG iteration step rather than

$$\frac{\left\|\boldsymbol{r}^{(k)}\right\|}{\|\boldsymbol{f}\|} \leq \varepsilon. \tag{31}$$

Although ε in Eq. (31) should be set to be smaller than τ in Eq. (10), ε in Eq. (30) can be set to be much larger than τ in Eq. (10). This is because Eq. (30) is more severe than Eq. (31). Here, $\left\|\boldsymbol{r}^{(0)}\right\|$ is generally smaller than $\|\boldsymbol{f}\|$. The changes of the initial guess and the convergence criterion are summarized in Fig. 4. The horizontal axes represent the accumulated PCG iteration step, k, whereas the vertical axes represent the relative residual norm, $\left\|\boldsymbol{r}^{(k)}\right\| / \|\boldsymbol{f}\|$. Three lines are drawn in each of Fig. 4 (a), (b) and (c). In Fig. 4 (a), it is indicated that the linear systems of equations are solved three times by the PCG solver. Each line begins with $\left\|\boldsymbol{r}^{(k)}\right\| / \|\boldsymbol{f}\| = 10^0$ and ends with $\left\|\boldsymbol{r}^{(k)}\right\| / \|\boldsymbol{f}\| \leq \varepsilon$. By changing the initial guess, $\boldsymbol{u}^{(0)}$, from the zero vector to the converged solution at the previous iteration step, the second and third lines in Fig. 4 (b) start with $\left\|\boldsymbol{r}^{(k)}\right\| / \|\boldsymbol{f}\| < 10^0$, because the converged solution at the previous iteration step would be nearer to the converged solution at the current iteration step than the zero vector. Moreover, by using Eq. (30) as the convergence criterion, all the three lines in Fig. 4 (c) end with $\left\|\boldsymbol{r}^{(k)}\right\| / \left\|\boldsymbol{r}^{(0)}\right\| \leq \varepsilon$. The effectiveness of these changes are demonstrated numerically in Subsection 3.3.

2.5. *Search for neighboring integration points*

The stress transfers in the coupling-matrix-free iterative s-FEM use the information of neighboring integration points. The information of neighboring integration points

is generated once before the iteration, and is used at every iteration step. In the local least squares interpolation, the integration points of the local mesh inside each element of the global mesh should be collected. In the nearest neighbor interpolation, the integration point of the global mesh near each integration point of the local mesh should be collected. Here, the linear search algorithm, which is the simplest search algorithm, can be considered. The linear search algorithm for the local least squares interpolation is described as follows.

for each integration point (element) of the global mesh, **do**
  for each integration point of the local mesh, **do**
    if the integration point of the local mesh is inside the element of the global mesh **then**
      Store the integration point of the local mesh as a neighbor of the integration point of the global mesh
    end if
  end for
end for

However, the computational cost of this algorithm is $O(n^{\mathrm{Global}} n^{\mathrm{Local}})$, where n^{Global} and n^{Local} are the numbers of integration points of the global and local meshes, respectively. Actually, the linear search algorithm spent 28,819 s, which was 87% of the total computational time, in the numerical experiment of Subsection 3.4. Therefore, a fast search algorithm is necessary.

A bucket search algorithm is frequently used in the particle methods to search for neighboring particles [Ferrari *et al.* (2009); Murotani *et al.* (2014b)]. Ideally, the computational cost of the bucket search algorithm is $O(n^{\mathrm{Global}})$ or $O(n^{\mathrm{Local}})$, in the search for integration points of the local or global meshes, respectively. This algorithm reduced the search process in the numerical experiment of Subsection 3.4 from 28,819 s to 8 s. Here, the bucket search algorithm for the coupling-matrix-free iterative s-FEM is explained. The buckets for the local least squares interpolation are shown in Fig. 5. First, an axis-aligned background grid, which is referred to as the buckets, is prepared. The shape of each bucket is a cube in three dimensions, or a square in two dimensions, whose size is the average element edge length of the local mesh. In each bucket, the integration points of the local mesh that are inside the bucket are stored in the compressed sparse row (CSR) graph format. Then, by using the buckets, the integration points of the local mesh that are inside each element of the global mesh are searched for. The element of the global mesh is shown in dark gray, and the search region is shown in light gray. The search region is determined by the maximum and minimum nodal coordinates of the element of the global mesh. For each integration point of the local mesh in the buckets that are marked by light gray, it is checked whether the integration point of the local mesh is inside the element of the global mesh. The algorithm of the bucket search for the local least squares interpolation is summarized as follows.

for each integration point of the local mesh, **do**

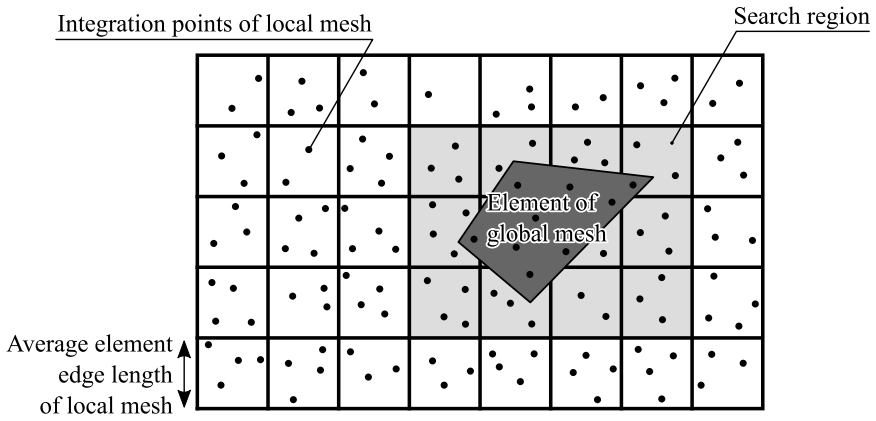

Fig. 5. Buckets to search neighboring integration points of the local mesh.

Store the integration point of the local mesh *into a bucket*
end for
for each integration point (element) of the global mesh, **do**
for each integration point of the local mesh *in the search-region buckets*, **do**
if the integration point of the local mesh is inside the element of the global mesh **then**
Store the integration point of the local mesh as a neighbor of the integration point of the global mesh
end if
end for
end for

Also, the bucket search algorithm for the nearest neighbor interpolation is very similar to this algorithm.

3. Numerical experiments

In the present study, two problems are analyzed using the coupling-matrix-free iterative s-FEM as well as the conventional FEM for comparison. The first problem is a simple stress concentration problem, which is a circular or elliptical hole in a flat plate. The accuracy and the convergence performance are investigated. It is also shown that the shape of the hole can be changed easily, whereas the global mesh remains unchanged. The second problem is a structure with a single hole or with multiple holes. We demonstrate that it is tractable to add holes in a structure. The computational time ratio from the conventional FEM to the coupling-matrix-free iterative s-FEM is roughly estimated based on the total number of PCG iteration counts in global analysis. This estimation is confirmed by measuring the computational time. Note that the number of iteration counts is reproducible, whereas the computational time itself depends strongly on the computer environment as

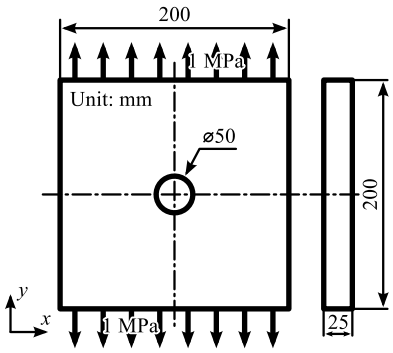

Fig. 6. Dimensions of a flat plate with a circular hole.

well as the programming approach. Although the coupling-matrix-free iterative s-FEM is always slower than the conventional FEM, the total time for the analyst to perform manual operation from pre-processing to post-processing would be shorter because the effort involved in mesh generation is extremely small. Furthermore, it is demonstrated that the position and the number of holes can be changed easily.

3.1. *Circular hole in a flat plate*

A flat plate with a circular hole subjected to a uniform remote tensile stress is analyzed. The accuracy of the stress concentration and the convergence performance of the coupling-matrix-free iterative s-FEM are investigated. The dimensions of the analysis model are shown in Fig. 6. The global and local meshes for the coupling-matrix-free iterative s-FEM are depicted in Figs. 7 and 8, respectively, and the mesh for the conventional FEM is depicted in Fig. 9. These meshes are visualized using AutoGL library [Kawai (2006)], which is based on OpenGL and GTK+. These meshes are 1/8 models because of their symmetry. The linear hexahedral finite element is adopted. Note that the circular hole is not modeled by the global mesh. The numbers of elements and nodes of the global mesh of Fig. 7 are 64 and 162, respectively. Those of the local mesh of Fig. 8 are 2,048 and 2,805, respectively. Those of Fig. 9 are 4,096 and 5,445, respectively. All of the nodes on the global–local interface, Γ^{GL}, of the local mesh are constrained by following Eq. (2). Young's modulus is set to be 210 GPa, and Poisson's ratio is set to be 0.3. The tolerance of the coupling-matrix-free iterative s-FEM, τ, in Eq (10) and that of the PCG solver, ε, in Eq. (30) are set to be 10^{-6} and 10^{-3}, respectively. Here, ε can be set to be much larger than τ, as described in Subsection 2.4.

The computed stress in the y direction is visualized in Figs. 10 and 11. Figure 10 is computed by coupling-matrix-free iterative s-FEM with the Aitken relaxation method. The elements of the global mesh inside the hole are not shown. The stress distribution from red to magenta near the hole edge appears well represented. Note that a stress oscillation is observed in the local mesh. This is because a Gaussian

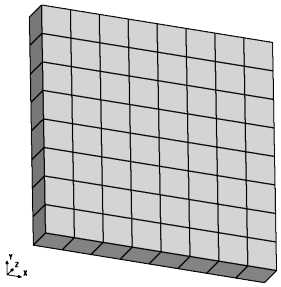

Fig. 7. Global mesh of the circular hole problem for s-FEM analysis.

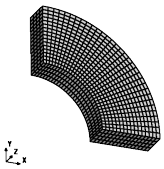

Fig. 8. Local mesh of the circular hole problem for s-FEM analysis.

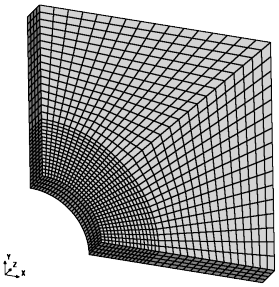

Fig. 9. Mesh of the circular hole problem for conventional FEM analysis.

quadrature with eight integration points on the global mesh is not sufficient to represent the discontinuous stress distribution across the element faces of the local mesh. This oscillation can be overcome in two-dimensional analysis by applying the sub-element quadrature technique to the global mesh [Yumoto *et al.* (2016b)]. It should be noted here that the goal of the present study is to demonstrate the capability of the coupling-matrix-free iterative s-FEM for three-dimensional analysis by accelerating the convergence. Further research should be performed in order to smooth the oscillation and establish an entirely accurate s-FEM solution in three-dimensional analysis. In three-dimensional analysis, mesh refinement techniques of tetrahedral elements [Murotani *et al.* (2014a)] may be helpful. The stress concentration in the vicinity of the circular hole at the center of thickness is plotted in Fig. 12. The horizontal axis represents the coordinate perpendicular to the y direction from the hole edge. The vertical axis represents the stress in the y direction normalized by the remote stress. The nodal values that are interpolated from the neighboring integration points are plotted. The results of the coupling-matrix-free iterative s-FEM and those of the conventional FEM are in good agreement in the sense that the stress concentration is well represented, even though the stress oscillation is observed in Fig. 10. Also, the theoretical normalized stress of a circular hole in an *infinite plate* is 3. The computed normalized stresses in Fig. 12 are slightly larger than 3, because the plate is finite.

The convergence performance of the coupling-matrix-free iterative s-FEM is investigated in detail. The convergence histories of the SOR method with various relaxation factors, ω, are plotted in Fig. 13. The horizontal axis represents the iteration step of the coupling-matrix-free iterative s-FEM, whereas the vertical axis represents the relative residual norm of the left-hand side of Eq. (10). This parametric study indicates that $\omega = 1.7$ is appropriate for this problem. The convergence histories of the Gauss–Seidel method with the fixed-point iteration method and static relaxation are plotted in Fig. 14. This parametric study establishes that $\omega = 1.9$ is appropriate. The convergence histories of all five methods considered in

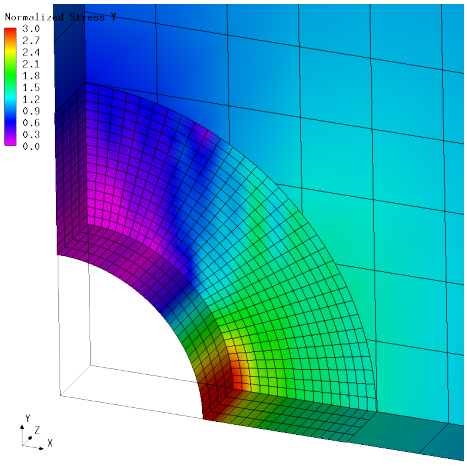

Fig. 10. Stress y of the circular hole problem the computed by coupling-matrix-free iterative s-FEM.

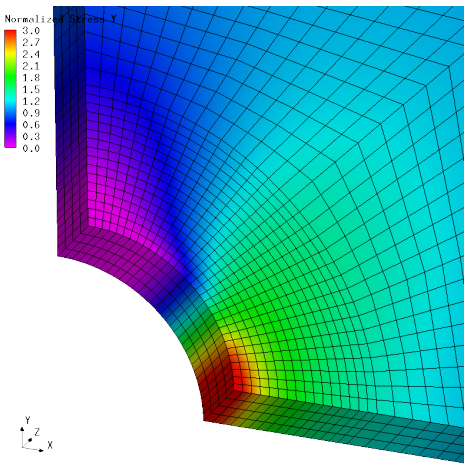

Fig. 11. Stress y of the circular hole problem computed by the conventional FEM.

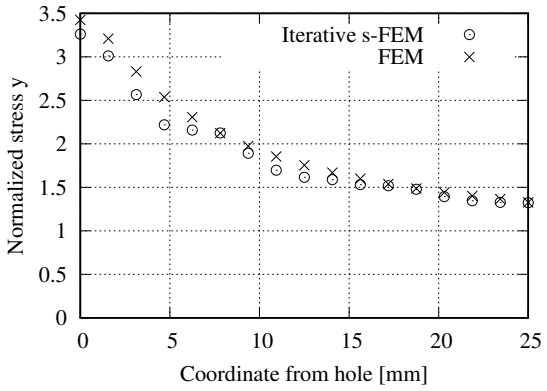

Fig. 12. Stress concentration in the vicinity of the circular hole of the circular hole problem.

the present study are shown in Fig. 15. Although the number of iteration counts of the SOR method with $\omega = 1.7$ is the smallest, nearly the best convergence performance can be achieved with the Aitken relaxation method, which does not require a parametric study. The Aitken relaxation method is approximately five times faster than that Gauss–Seidel method, which is the straightforward method. It is demonstrated that the Aitken relaxation method estimates optimal ω. Note that the computational time of this numerical experiment is too small to investigate the effectiveness of the present method. The computational time of more large-scale problems in Subsections 3.3 and 3.4 is measured.

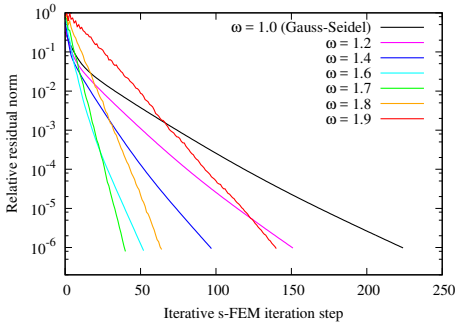

Fig. 13. Convergence histories of the SOR method for the circular hole problem.

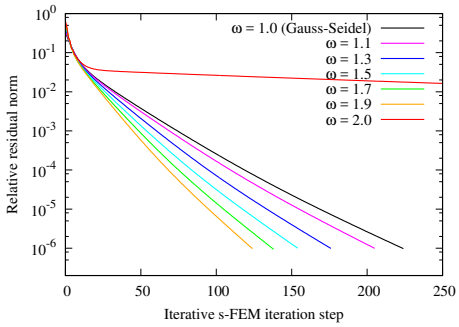

Fig. 14. Convergence histories of the Gauss–Seidel method with relaxation for the circular hole problem.

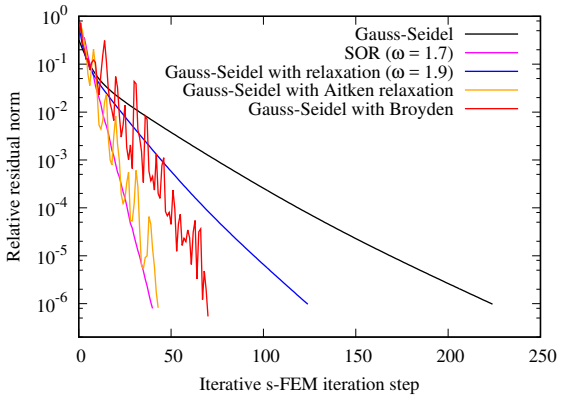

Fig. 15. Convergence histories of the coupling-matrix-free iterative s-FEM analysis for the circular hole problem.

3.2. *Elliptical hole in a flat plate*

A flat plate with an elliptical hole subjected to a uniform remote tensile stress is analyzed in order to demonstrate that the shape of the hole can easily be changed. The results of the computed stresses and the convergence performance of Aitken-based coupling-matrix-free iterative s-FEM are investigated in this subsection. Although the dimensions of the analysis model are the same as those of the previous section, which is shown in Fig. 6, the shape of the hole is different. The axis in the horizontal direction remains 25 mm, whereas that in the vertical direction changes. The axes of 35 mm and 15 mm in the vertical direction are analyzed. The linear hexahedral finite element is adopted again. The total numbers of elements and nodes are the same as in the circular hole problem. Only the nodal coordinates of the local mesh are transformed to represent the elliptical hole. Young's modulus is set to be 210

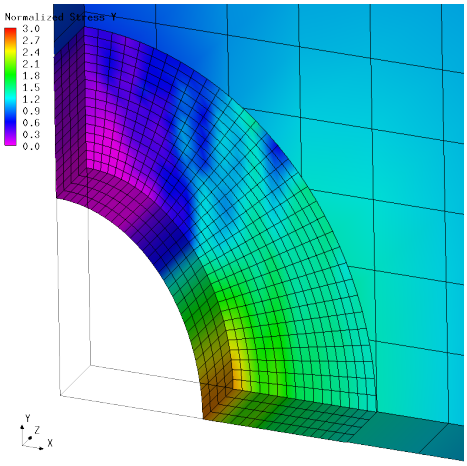

Fig. 16. Stress y of the elliptical hole problem of the 35-mm axis in the vertical direction computed by the coupling-matrix-free iterative s-FEM.

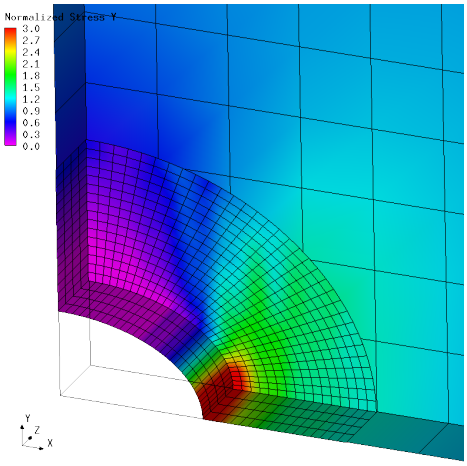

Fig. 17. Stress y of the elliptical hole problem of the 15-mm axis in the vertical direction computed by the coupling-matrix-free iterative s-FEM.

GPa, and Poisson's ratio is set to be 0.3.

The distributions of the stress in the y direction along with the mesh discretization computed by the Aitken-based coupling-matrix-free iterative s-FEM are visualized in Figs. 16 and 17. The elements of the global mesh inside the hole are not shown. The stress concentration of each elliptical hole problem appears to be well represented. Note that stress oscillations are also observed in the elliptical hole problems. The stress concentration in the vicinity of the elliptical hole at the center of thickness is plotted in Fig. 18. The horizontal axis represents the coordinate from the elliptical hole, whereas the vertical axis represents the stress in the y direction normalized by the remote stress. As the axis of the elliptical hole in the vertical direction becomes smaller, the stress concentrates severely. Also, the theoretical normalized stresses of a elliptical hole in an *infinite plate* are 2.43 ($a = 25$ mm and $b = 35$ mm) and 4.33 ($a = 25$ mm and $b = 15$ mm). The computed normalized stresses in Fig. 18 are slightly larger than these values, because the plate is finite.

Convergence histories of the coupling-matrix-free iterative s-FEM with the Gauss–Seidel method, the Aitken relaxation method and the Broyden method are plotted in Figs. 19 and 20. The horizontal axes represent the iteration step, whereas the vertical axes represent the relative residual norm of the left-hand side of Eq. (10). The Aitken relaxation method exhibited the best convergence performance, and the Broyden method exhibited the second best convergence performance. This tendency is similar to that of the numerical experiment in the previous subsection. For all axes of the elliptical hole in the vertical direction, the numbers of iteration counts are similar. The numbers of iteration counts appear to increase slightly as the axis

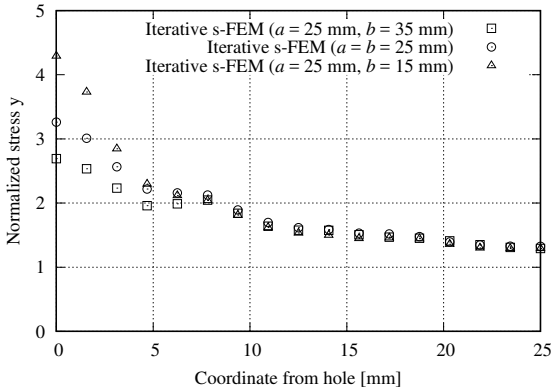

Fig. 18. Stress concentration in the vicinity of the elliptical hole of the elliptical hole problems computed by the coupling-matrix-free iterative s-FEM.

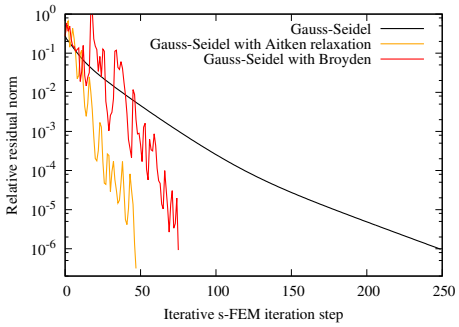

Fig. 19. Convergence histories of the coupling-matrix-free iterative s-FEM analysis for the elliptical hole problem of the 35-mm axis in the vertical direction.

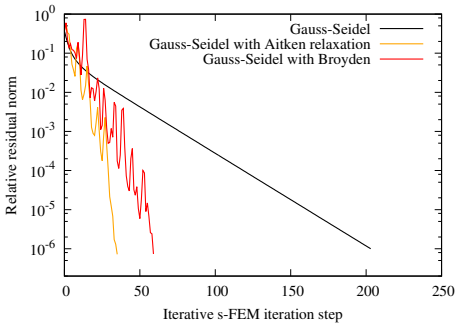

Fig. 20. Convergence histories of the coupling-matrix-free iterative s-FEM analysis for the elliptical hole problem of the 15-mm axis in the vertical direction.

of the elliptical hole in the vertical direction becomes larger. Note that the computational time of this numerical experiment is too small to investigate the effectiveness of the present method. The computational time of more large-scale problems in Subsections 3.3 and 3.4 is measured.

3.3. *Circular hole in a turbine blade structure*

A section of the gas turbine blade with a circular hole is analyzed. We demonstrate that it is tractable to add a hole in a realistic mechanical component. The computational time ratio from the conventional FEM without the hole to the coupling-matrix-free iterative s-FEM with a hole is roughly estimated from the total number of PCG iteration counts. This ratio indicates how long it takes to obtain the results

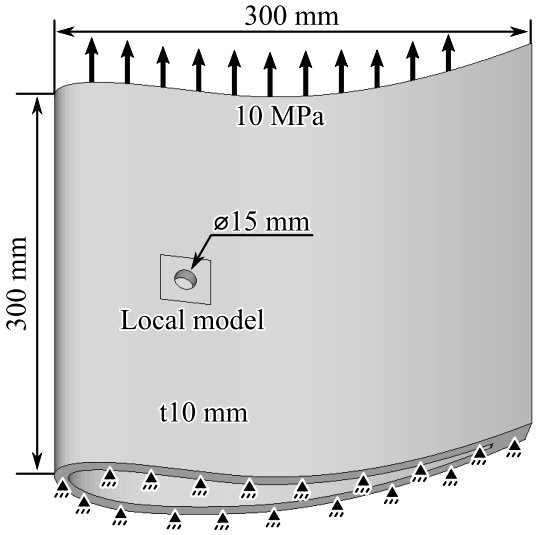

Fig. 21. Dimensions and boundary conditions of a turbine blade structure with a circular hole.

when a hole is added. The dimensions and the boundary conditions are shown in Fig. 21. A circular hole having a diameter of 15 mm is located at the center of the turbine blade. The global and local meshes, and the enlarged local mesh are depicted in Figs. 22 and 23, respectively. The quadratic tetrahedral finite element is adopted for the global mesh, and the linear hexahedral finite element is adopted for the local mesh. This is because the tetrahedral elements are preferable for a three-dimensional complex-shaped structure, and the hexahedral elements are preferable for a simple-shaped model. As described in Subsection 2.2, we can use two different kinds of finite elements together in the coupling-matrix-free iterative s-FEM. The numbers of elements and nodes of the global mesh are 97,920 and 163,108, respectively, and those of the local mesh are 16,384 and 19,584, respectively. All nodes on the global–local interface, Γ^{GL}, of the local mesh are constrained following Eq. (2). Young's modulus is set to be 210 GPa, and Poisson's ratio is set to be 0.3. The tolerance of the coupling-matrix-free iterative s-FEM, τ, in Eq (10) and that of the PCG solver, ε, in Eq. (30) are set to be 10^{-6} and 10^{-3}, respectively. A computer having an Intel Core i5-4590 (Haswell Refresh) CPU with DDR3 SDRAM PC-12800 was used. The operation system is Ubuntu 16.04 LTS and the compiler is GNU Compiler Collection (`gcc`) 5.4 with its options of `-std=c99 -fopenmp -O2`. The number of OpenMP threads is four.

The equivalent stress computed by the coupling-matrix-free iterative s-FEM with a circular hole is visualized in Fig. 24, and that computed by the conventional FEM without a circular hole is visualized in Fig. 25. The equivalent stress

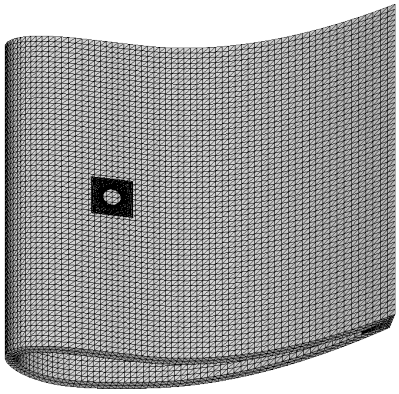

Fig. 22. Global and local meshes of a turbine blade structure with a circular hole.

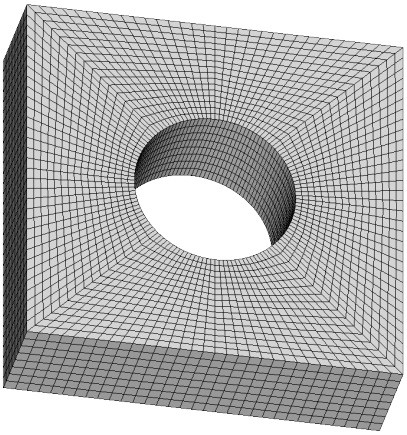

Fig. 23. Local mesh of a turbine blade structure with a circular hole.

of Fig. 24 near the circular hole is depicted in Fig. 26. The stress concentration on the right-hand side of the hole and at the center of thickness is plotted in Fig. 27. The horizontal axis represents the coordinate perpendicular to the tensile direction from the hole edge, whereas the vertical axis represents the equivalent stress. The nodal values interpolated from the neighboring integration points are plotted. The reference solution, σ^{ref}, is the formula of a circular hole in an *infinite flat plate* under a plane stress state, which is expressed as

$$\sigma^{\mathrm{ref}} = \sqrt{{\sigma_x^{\mathrm{ref}}}^2 + {\sigma_y^{\mathrm{ref}}}^2 - \sigma_x^{\mathrm{ref}}\sigma_y^{\mathrm{ref}} + 3\sigma_{xy}^{\mathrm{ref}}}, \tag{32}$$

$$\sigma_x^{\mathrm{ref}} = \sigma_0 \left(\frac{3}{2}\frac{a^2}{r^2} - \frac{3}{2}\frac{a^4}{r^4} \right), \tag{33}$$

$$\sigma_y^{\mathrm{ref}} = \sigma_0 \left(1 + \frac{1}{2}\frac{a^2}{r^2} + \frac{3}{2}\frac{a^4}{r^4} \right), \tag{34}$$

$$\sigma_{xy}^{\mathrm{ref}} = 0, \tag{35}$$

where σ_0 is the remote stress, a is the radius of the circular hole, and r is the coordinate from the center of the circular hole. The circular hole appears to be well modeled in the turbine blade structure, in the sense that the stress concentration is accurately represented.

Next, we discuss the computational time of the proposed coupling-matrix-free iterative s-FEM. Due to the solution procedures of the present method, the computational time can be considered to be proportional to the total number of iteration counts of the PCG solver. First, the convergence histories of the Gauss–Seidel

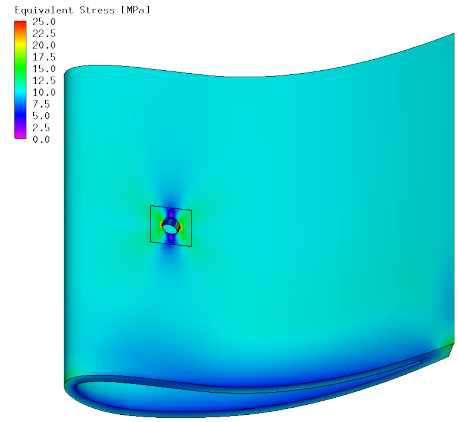

Fig. 24. Equivalent stress of the turbine blade structure problem computed by the coupling-matrix-free iterative s-FEM.

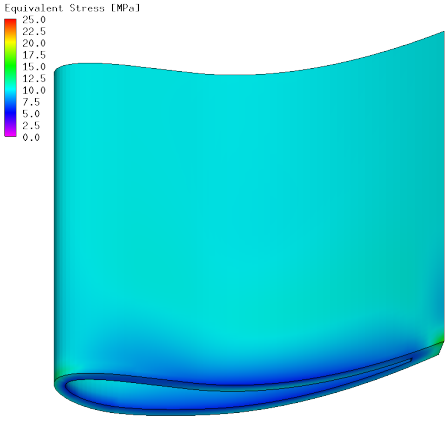

Fig. 25. Equivalent stress of the turbine blade structure problem without a circular hole computed by the conventional FEM.

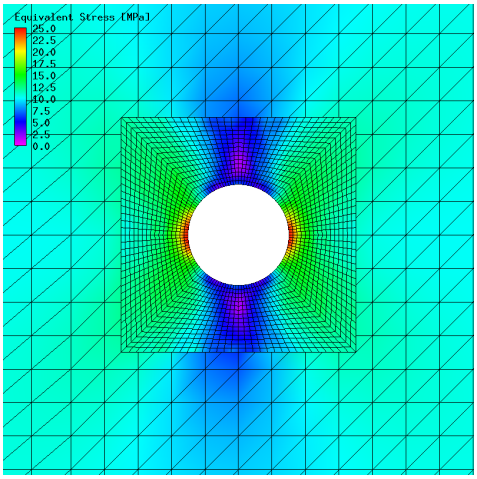

Fig. 26. Equivalent stress near the circular hole of the turbine blade structure problem.

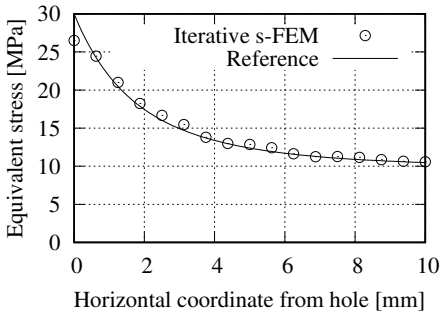

Fig. 27. Stress concentration in the vicinity of the circular hole of the turbine blade structure problem.

method, the Aitken relaxation method, and the Broyden method are plotted in Fig. 28. The horizontal axis represents the iteration step of the coupling-matrix-free iterative s-FEM, whereas the vertical axis represents the relative residual norm of the left-hand side of Eq. (10). The numbers of iteration counts were 593, 59 and 170 in order. The Aitken relaxation method exhibited the best convergence performance, and the Broyden method exhibited the second best convergence performance. The

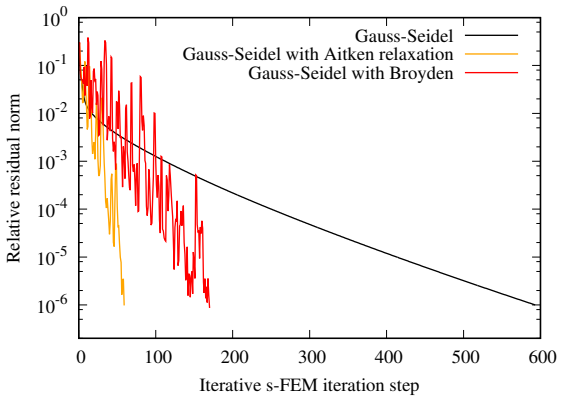

Fig. 28. Convergence histories of the coupling-matrix-free iterative s-FEM analysis for the turbine blade structure problem with a hole.

convergence history of the PCG solver in the Aitken-based coupling-matrix-free iterative s-FEM is shown in Fig. 29, and that of the conventional FEM without a circular hole is shown in Fig. 30 for comparison. The horizontal axes represent the PCG iteration step, whereas the vertical axes represent the relative residual norm. In the Aitken-based coupling-matrix-free iterative s-FEM, the PCG solver was called 59 times due to 59 iteration counts. Thus, 59 lines are plotted successively in Fig. 29. The numbers of PCG iteration counts are shown in Fig. 31. All numbers are much smaller than that of PCG iteration counts of the conventional FEM (Fig. 30), as indicated by the dotted line, owing to the effective use of linear solvers described in Subsection 2.4. The numbers of total PCG iteration counts in Figs. 29 and 30 are 20,357 and 4,440, respectively. The ratio between the total PCG iteration counts is 4.58, which means that the computational time of the coupling-matrix-free iterative s-FEM is estimated to be 4.58 times larger than that of the conventional FEM, even though the number of iteration counts of the coupling-matrix-free iterative s-FEM is 59. The speedup from 59 to 4.58 is due to the effective use of linear solvers. Here, the measured computational time of the coupling-matrix-free iterative s-FEM was 1,689 s, and that of the conventional FEM without a circular hole was 363 s. The measured computational time ratio was 4.65. The estimation based on the number of total PCG iteration counts of global analysis was successfully confirmed to be appropriate. Note that the measured computational time itself depends strongly on the computer environment as well as the programming approach.

3.4. *Multiple circular holes in a turbine blade structure*

A section of gas turbine blade with 18 holes is analyzed in order to demonstrate that the position and the number of holes can easily be changed. Although the dimensions and boundary conditions are the same as those in the previous subsection, as shown

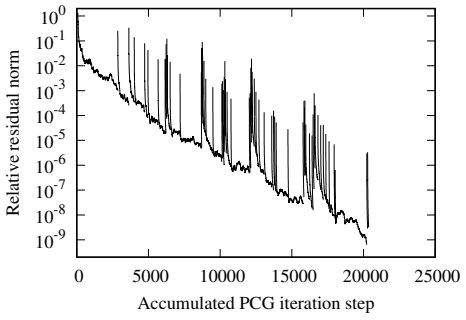

Fig. 29. Convergence histories of the PCG solver in the coupling-matrix-free iterative s-FEM with Aitken relaxation for the turbine blade structure problem with a hole.

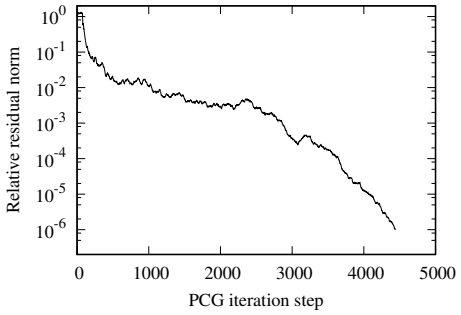

Fig. 30. Convergence history of the PCG solver in the conventional FEM for the turbine blade structure problem without a hole.

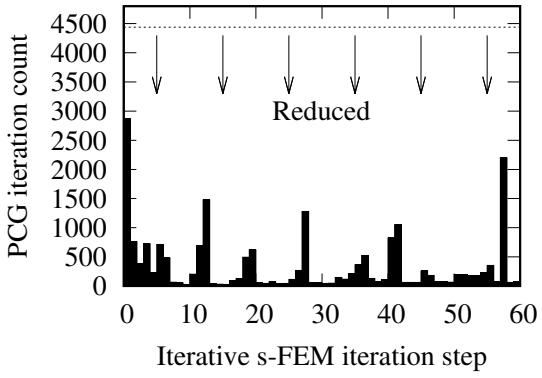

Fig. 31. Numbers of PCG iteration counts of the coupling-matrix-free iterative s-FEM analysis with Aitken relaxation for the turbine blade structure problem with a hole.

in Fig. 21, 18 circular holes of 15 mm in diameter are placed. The global and local meshes are depicted in Fig. 32. The adopted finite element types and the numbers of elements and nodes remain the same. The numbers of elements and nodes of each local mesh are the same, and only the nodal coordinates are different. The numbers of elements and nodes of the global mesh are 97,920 and 163,108, respectively, and those of the local mesh are 294,912 and 352,512, respectively. Since the number of nodes of the local mesh is very large, the PCG solver rather than the LDL factorization solver was used in the local analyses. Note that the multiple local meshes are regarded as one mesh in the present study, although it is possible to analyze the multiple local meshes separately in completely parallel computing. Young's modulus is set to be 210 GPa, and Poisson's ratio is set to be 0.3.

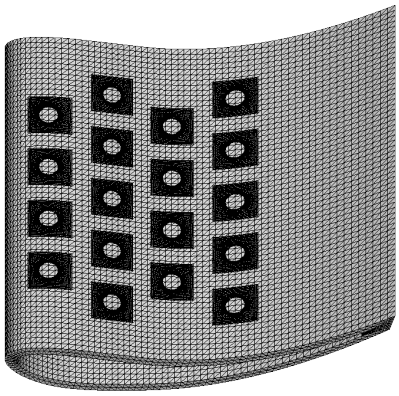

Fig. 32. Global and local meshes of a turbine blade structure with 18 circular holes.

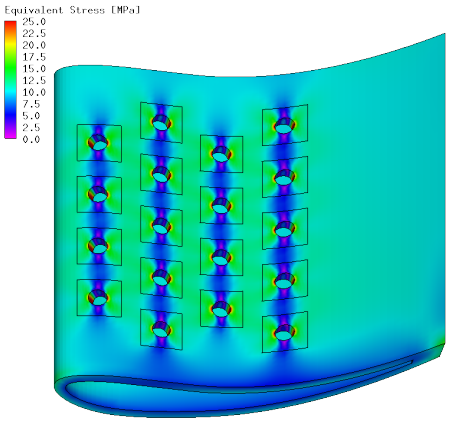

Fig. 33. Equivalent stress of the multi-hole turbine blade structure problem computed by the coupling-matrix-free iterative s-FEM.

The equivalent stress computed by the coupling-matrix-free iterative s-FEM is visualized in Fig. 33. An enlarged view is shown in Fig. 34. The stress appears to have been analyzed successfully, even in the case of multiple holes. The stress concentration on the right-hand side of the hole whose position is the same as that in the previous subsection is plotted in Fig. 35. The horizontal axis represents the coordinate perpendicular to the tensile direction from the hole edge, whereas the vertical axis represents the equivalent stress. The reference solution is the same as that in the previous section, which is given by Eq. (32). The stress concentration is accurately represented even though there are multiple holes in the structure. Since the computed equivalent stress of Fig. 35 is slightly larger than that of Fig. 27, the holes appear to interact with each other.

Next, we discuss the number of iteration counts in relation with the computational time in a similar manner to the previous subsection. The convergence histories of the Gauss–Seidel method, the Aitken relaxation method and the Broyden method are plotted in Fig. 36. The horizontal axis represents the iteration step of the coupling-matrix-free iterative s-FEM, whereas the vertical axis represents the relative residual norm of the left-hand side of Eq. (10). The numbers of iteration counts were 692, 94 and 227 in order. The number of total PCG iteration counts of the global analyses was 40,464. That of the conventional FEM was 4,440. The ratio between the total PCG iteration counts is 9.11. Here, the measured computational time of the coupling-matrix-free iterative s-FEM and the conventional FEM were 4,183 s and 363 s, respectively. The measured computational time ratio was 11.52. The slight difference between 9.11 and 11.52 is because the computational cost of the local analyses can not be ignored. The number of nodes of the local mesh is

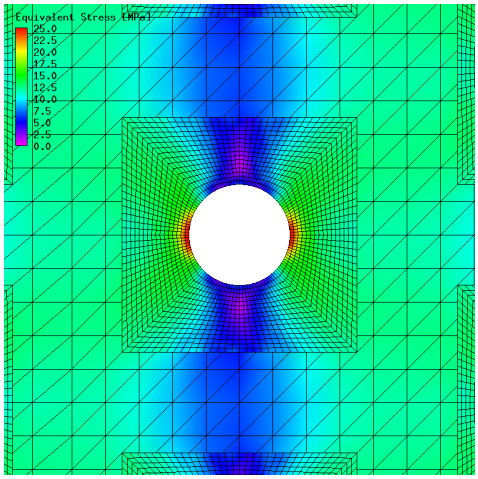

Fig. 34. Equivalent stress near the circular holes of the multi-hole turbine blade structure problem.

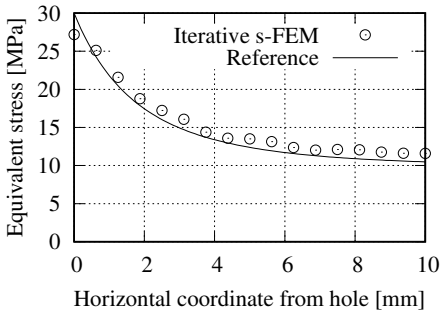

Fig. 35. Stress concentration in the vicinity of the circular holes of the multi-hole turbine blade structure problem.

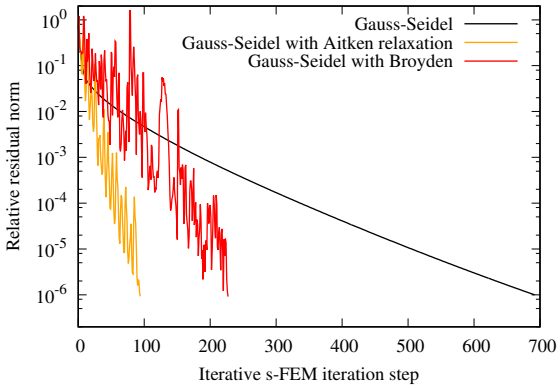

Fig. 36. Convergence histories of the coupling-matrix-free iterative s-FEM analysis for the multi-hole turbine blade structure problem.

approximately two times larger than that of the global mesh.

4. Conclusion

In the present paper, three-dimensional elastic problems with a single hole and multiple holes are analyzed effectively by the coupling-matrix-free iterative s-FEM with acceleration techniques. The present method enables us to perform three-dimensional s-FEM analysis very easily, because the generations of coupling stiffness matrices are completely eliminated. Troublesome three-dimensional numerical inte-

gration for a volume of partly overlapping finite elements, which is required in order to generate coupling stiffness matrices, is no longer needed. The coupling is now evaluated by stress transfers between global and local meshes. These procedures can be applied to any kinds of finite elements. We used hexahedral finite elements for the local mesh and tetrahedral finite elements for the global mesh in the numerical experiments. No additional techniques are required in order to deal with the use of a mixture of hexahedral and tetrahedral finite elements. In order to model a hole in a structure by the coupling-matrix-free iterative s-FEM, the straightforward algorithm, which is based on the Gauss–Seidel method, requires several hundred iteration counts. This means that the coupling-matrix-free iterative s-FEM with a hole is several hundred times slower than the conventional FEM without a hole. The convergence acceleration techniques based on the Aitken relaxation method reduce the computational time by approximately ten times, and the use of linear solvers for changing the procedures the initial guess and the convergence criterion reduces the computational time by approximately ten times. The computational time ratio of the turbine blade structure model from the conventional FEM without a hole to the accelerated coupling-matrix-free iterative s-FEM with a hole was estimated to be 4.58 based on the numbers of total PCG iteration counts and was measured to be 4.65, whereas the straightforward algorithm based on the Gauss–Seidel method requires 593. The convergence acceleration techniques based on the Aitken relaxation method reduced 593 to 59. Then, the use of linear solvers reduced 59 to 4.58. Although the accelerated coupling-matrix-free iterative s-FEM is several times slower than the conventional FEM, the amount of manual operation of the analyst from pre-processing to post-processing would be shorter because the effort involved in mesh generation is extremely small. The present method enables us to easily add a hole, holes, cracks, etc., in a structure. Also, commercial FEM software may be applicable to the global and local analyses by developing appropriate interfaces. Sophisticated features in the commercial FEM software, such as high-performance elements, multi-point constraints and contact, can be used in s-FEM analysis.

In future, the coupling-matrix-free iterative s-FEM will be applied to many-hole problems and to nonlinear problems, such as problems involving elastic–plastic materials and large-deformation phenomena. For the former problems, a number of local meshes are used, and these would partly overlap each other. The interactions between the local meshes should be considered. For the latter problems, a nonlinear solution methodology would be able to be optimized for the coupling-matrix-free iterative s-FEM, because the present method itself includes nonlinear solution algorithms.

Acknowledgements

The present study was supported in part by a Grant-in-Aid for Scientific Research (C) (No. 16K05988) from the Japan Society for the Promotion of Science.

References

Arai, K., Yodo, K., Okada, H., Yamada, T., Kawai, H., and Yoshimura, S. (2015). Ultra-large scale fracture mechanics analysis using a parallel finite element method with submodel technique. *Finite Elem. Anal. Des.*, **105**: 44–55.

Ferrari, A., Dumbser, M., Toro, E. F., and Armanini, A. A new 3D parallel SPH scheme for free surface flows. *Comput. Fluids*, **38** (6): 1203–1217.

Fish, J. (1992). The s-version of the finite element method. *Comput. Struct.*, **43** (3): 539–547.

Fish, J. and Markolefas, S. (1993). Adaptive s-method for linear elastostatics. *Comput. Methods Appl. Mech. Eng.*, **104** (3): 363–396.

Fish, J., Markolefas, S., Guttal, R., and Nayak, P. (1994) On adaptive multilevel superposition of finite element meshes for linear elastostatics. *Appl. Numer. Math.*, **14** (1): 135–164.

Fish, J. and Guttal, R. (1996). The s-version of finite element method for laminated composites. *Int. J. Numer. Methods Eng.*, **39** (21): 3641–3662.

Grm, A. and Batista, M. (2016). On the coupling of analytical and FEM solution in stress analysis around the polygonal hole shape in a finite two-dimensional domain. *Int. J. Mech. Sci.*, *118*: 254–67.

Han, Z. D. and Atluri, S. N. (2002). SGBEM (for cracked local subdomain)–FEM (for uncracked global structure) alternating method for analyzing 3D surface cracks and their fatigue-growth. *Comput. Model. Eng. Sci.*, **3** (6): 699–716.

Hughes, T. J. R., Cottrell, J. A., Bazilevs, Y. (2005). Isogeometric analysis: CAD, finite elements, NURBS, exact geometry and mesh refinement. *Comput. Methods Appl. Mech. Eng.*, **194**: 4135–4195.

Kamaya, M., Miyokawa, E., Kikuchi, M. (2010). Growth prediction of two interacting surface cracks of dissimilar sizes. *Eng. Fract. Mech.*, **77** (16): 3120–3131.

Kawagai, M., Sando, A., and Takano, N. (2006). Image-based multi-scale modelling strategy for complex and heterogeneous porous microstructures by mesh superposition method. *Model. Simul. Mater. Sci. Eng.*, **14** (1): 53–69.

Kawai, H. ADVENTURE AutoGL: A handy graphics and GUI library for researchers and developers of numerical simulations. *Comput. Model. Eng. Sci.*, **11** (3): 111–120.

Kelley, C. T. (2003). *Solving Nonlinear Equations with Newton's Method*. Society for Industrial and Applied Mathematics.

Kikuchi, M., Wada, Y., and Takahashi, M. Fatigue crack growth simulation using s-FEM. *Trans. Jpn. Soc. Mech. Eng. Ser. A*, **74** (742): 812–818.

Kikuchi, M., Wada, Y., Shintaku, Y., Suga, K., and Li, Y. (2014). Fatigue crack growth simulation in heterogeneous material using s-version FEM. *Int. J. Fatigue*, **58**: 47–55.

Lee, S. H., Song, J. H., Yoon, Y. C., Zi, G., and Belytschko, T. (2004). Combined extended and superimposed finite element method for cracks. *Int. J. Numer. Methods Eng.*, **59** (8): 1119–1136.

Maitireyimu, M., Kikuchi, M., and Geni, M. Comparison of experimental and numerically simulated fatigue crack propagation. *J. Solid Mech. Mater. Eng.*, **3** (7): 952–967.

Minami, S. and Yoshimura, S. Practical performances of non-linear algorithms for partitioned iterative method of fluid–structure interaction problems. *J. Comput. Sci. Tech.*, **3** (1): 396–407.

Minami, S. and Yoshimura, S. (2010). Performance evaluation of nonlinear algorithms with line-search for partitioned coupling techniques for fluid–structure interactions. *Int. J. Numer. Methods Fluids*, **64** (10–12): 1129–47.

Miyamura, T., Noguchi, H., Shioya, R., Yoshimura, S., and Yagawa, G. (2001). Elastic–plastic analysis of nuclear structures with millions of DOFs using the hierarchical

domain decomposition method. *Nucl. Eng. Des.*, **212** (1–3): 335–355.

Murotani, K., Sugimoto, S., Kawai, H., and Yoshimura, S. (2014a). Hierarchical domain decomposition with parallel mesh refinement for billions-of-DOF scale finite element analyses. *Int. J. Comput. Methods*, **11** (3): 1350061 (30 pages).

Murotani, K., Koshizuka, S., Tamai, T., Shibata, K., Mitsume, N., Yoshimura, S., Tanaka, S., Hasegawa, K., Nagai, E., and Fujisawa, T. (2014b). Development of hierarchical domain decomposition explicit MPS method and application to large-scale tsunami analysis with floating objects. *J. Adv. Simul. Sci. Eng.*, **1** (1): 16–35.

Nakasumi, S., Suzuki, K., Fujii, D., Ohtsubo, H. (2003). Mixed analysis of shell and solid elements using the overlaying mesh method. *J. Marine Sci. Tech.*, **7** (4): 180–188.

Nakasumi, S., Suzuki, K., and Ohtsubo, H. (2008). Crack growth analysis using mesh superposition technique and X-FEM. *Int. J. Numer. Methods Eng.*, **75** (3): 291–304.

Nikishkov, G. P., Park, J. H., and Atluri, S. N. (2001). SGBEM–FEM alternating method for analyzing 3D non-planar cracks and their growth in structural components. *Comput. Model. Eng. Sci.*, **2** (3): 401-422.

Nishikawa, H., Serizawa, H., and Murakawa, H. (2007). Actual application of FEM to analysis of large scale mechanical problems in welding. *Sci. Tech. Weld. Join.*, **12** (2): 147–152.

Okada, H., Liu, C. T., Ninomiya, T., Fukui, Y., and Kumazawa, N. (2004). Analysis of particulate composite materials using an element overlay technique. *Comput. Model. Eng. Sci.*, **6** (4): 333–348.

Okada, H., Endoh, S., and Kikuchi, M. (2005). On fracture analysis using an element overlay technique. *Eng. Fract. Mech.*, **72** (5): 773-789.

Okada, H., Endoh, S., and Kikuchi, M. (2007). Application of s-version finite element method to two-dimensional fracture mechanics problems. *J. Solid Mech. Mater. Eng.*, **1** (5): 699–710.

Sando, A. (2011a). Numerical integration for interactive terms in mesh superposition method by auto-mesh generation. *Trans. Jpn. Soc. Mech. Eng. Ser. A*, **77** (776): 600–609.

Sando, A. (2011b) Study on appropriate decomposition procedure of integral domain for high accurate numerical integration of interactive terms in finite element mesh superposition method by auto-mesh generation. *Trans. Jpn. Soc. Comput. Eng. Sci.* 20110011.

Suzuki, K., Ohtsubo, H., Min, S., and Shiraishi, T. Multi scale analysis of ship structure using overlaying mesh method. *Trans. Jpn. Soc. Comput. Eng. Sci.*, 19990020.

Suzuki, K., Ohtsubo, H., Nakasumi, S., Shinmura, D. (2002). Global local iterative analysis using overlaying mesh method. *J. Soc. Nav. Arch. Jpn.*, **192**: 691–696.

Takano, N. and Okuno, Y. (2004). Three-scale finite element analysis of heterogeneous media by asymptotic homogenization and mesh superposition methods. *Int. J. Solids Struct.*, **41** (15): 4121–4135.

Tanaka, S., Okada, H., Watanabe, Y., and Wakatsuki, T. (2006). Applications of s-FEM to the problems of composite materials with initial strain-like terms. *Int. J. Multiscale Comput. Eng.*, **4** (4): 411–428.

Wada, Y., Kikuchi, M., Yamada, S., Serizawa, R., and Li, Y. (2014). Fatigue growth of internal flaw: Simulation of subsurface crack penetration to the surface of the structure. *Eng. Fract. Mech.*, **123**: 100–115.

Yumoto, Y., Yusa, Y., and Okada, H. (2016). An s-version finite element method without generation of coupling stiffness matrix by using iterative technique. *Mech. Eng. J.*, **3** (5): 16-00001.

Yumoto, Y., Yusa, Y., and Okada, H. (2016). Element subdivision technique for coupling-

matrix-free iterative s-version FEM and investigation of sufficient element subdivision. *Mech. Eng. J.*, **3** (5): 16-00361.

Yusa, Y. and Yoshimura, S. (2013). Mixed-mode fracture mechanics analysis of large-scale cracked structures using partitioned iterative coupling method. *Comput. Model. Eng. Sci.*, **91** (6): 445-461.

Yusa, Y. and Yoshimura, S. Speedup of elastic–plastic analysis of large-scale model with crack using partitioned coupling method with subcycling technique. *Comput. Model. Eng. Sci.*, **99** (1): 87–104.

Zhang, Z., Wu, J., Zhang, S., Wang, M., Guo, R., and Guo, S. (2016). A new iterative method for springback control based on theory analysis and displacement adjustment. *Int. J. Mech. Sci.*, **105**: 330-339.